J Mater Sci (2010) 45:3215–3227
DOI 10.1007/s10853-010-4329-3

Synthesis of cobalt-doped barium cerate-zirconate and its evaluation for hydrogen production and electrochemical characterization

Aravind Suresh · Joysurya Basu · C. Barry Carter · Nigel Sammes · B. A. Wilhite

Received: 24 September 2009 / Accepted: 16 February 2010 / Published online: 2 March 2010
© Springer Science+Business Media, LLC 2010

Abstract Cobalt-doped barium cerate-zirconate was synthesized using an oxalate co-precipitation route. The material was characterized using X-ray diffraction, transmission and scanning transmission electron microscopy coupled with X-ray energy dispersive spectroscopy. Results indicated that homogeneous cubic phase material was obtained at very high heat-treatment temperatures. Catalytic activity of the material toward CH_3OH partial-oxidation was tested at different temperatures and O_2:CH_3OH ratios. High hydrogen yields were obtained indicating that the material was a suitable catalyst for hydrogen generation. Impedance spectroscopy tests were conducted at different conditions to understand conduction processes occurring in the material. Results suggested mixed protonic–electronic conductivity in the presence of hydrogen. Thus, material is a potential candidate for the bi-functional role of electroceramic catalyst for simultaneous hydrogen generation and purification.

A. Suresh · J. Basu · C. B. Carter · B. A. Wilhite (✉)
Department of Chemical, Materials and Bio-molecular Engineering, University of Connecticut, 191 Auditorium Road, Storrs, CT 06269, USA
e-mail: bwilhite@engr.uconn.edu

A. Suresh
e-mail: aravind.suresh@uconn.edu

J. Basu
e-mail: jbasu@engr.uconn.edu

C. B. Carter
e-mail: cbcarter@engr.uconn.edu

A. Suresh · J. Basu · C. B. Carter · B. A. Wilhite
Center for Clean Energy Engineering, University of Connecticut, 44 Weaver Road, Storrs, CT 06269, USA

N. Sammes
Department of Metallurgical and Materials Engineering, Colorado School of Mines, Golden, CO 80401, USA
e-mail: nsammes@mines.edu

Introduction

Burgeoning energy needs, diminishing fossil-fuel resources, and growing environmental concerns have motivated the development of multiple renewable fuels (e.g., biogas fermentation, alcohols) derived from diverse local and regional sources. Likewise, hydrogen has emerged as a universal energy currency [1] which can be harvested from hydrocarbons via any catalytic reaction (e.g., oxidative reforming) and converted to electrical energy directly by polymer electrolyte membrane fuel cells (PEMFCs), thus removing the Carnot-cycle limit on combustion efficiency [2]. However, by-products of reforming reactions include oxides of carbon and other contaminants. Trace amounts (10–100 ppm) of CO adversely affect operation of PEMFCs by catalyst poisoning [3]. CO_2 has also been reported to affect PEMFC performance by the formation of CO through a reverse water gas shift reaction with adsorbed hydrogen at the fuel cell anode [4]. Thus, efficient and cost-effective generation of high-purity hydrogen from hydrocarbons by catalytic reaction coupled with gas separation remains a critical challenge to the development of a hydrogen economy.

High-purity hydrogen production has been demonstrated using Pd membrane reactors, which integrate hydrogen generation and purification in parallel within a single stage [5, 6]. Practical application of this technique has been limited by high cost of Pd [7], loss of perm-selectivity owing to corrosion upon exposure to CH_3OH [8] and decreased hydrogen permeability upon exposure to CO and H_2O [9, 10]. The latter limitations can be mitigated by

coating a catalytic layer over the Pd perm-selective film [8, 11]. However, utilizing a Pd-membrane reactor for coupling hydrogen generation and purification is still limited by the onset of membrane instability above 500 °C [12]. Such instability can be a significant drawback given temperatures preferred for the catalytic reforming reactions of C_2H_5OH and higher hydrocarbons (400–1000 °C) [13].

To overcome limitations of Pd-based hydrogen perm-selective materials, the present research aims to identify a *single homogeneous material* capable of both hydrogen generation and purification. The target material is a high temperature electro-ceramic with dual functionality; (i) catalytic activity for hydrogen generation from CH_3OH via oxidative reforming; (ii) mixed protonic–electronic conductivity for electrochemical (non-galvanic) hydrogen purification. Whereas hydrogen is transported through Pd by surface dissociation of molecular hydrogen followed by dissolution and diffusion of atomic hydrogen through the film [14], the mechanism of hydrogen transport through high-temperature mixed protonic–electronic conductors involves electrochemical oxidation of hydrogen at the surface, conduction of protons and electrons in parallel through a dense film, followed by recombination at the other side. Electro-ceramics with dual functionality provide an opportunity for directly coupling hydrogen generation and purification at the electro-ceramic surface, for both Faradaic and non-Faradaic enhancement of reaction rates. This is especially of interest, as these enhancements in fuel-reforming rates and hydrogen yields are beyond the classical benefits in performance associated with conventional membrane reactors owing to Le Chatelier's principle [15].

Proton conductivity in aliovalent-cation-doped $SrCeO_3$ perovskites at high temperatures under hydrogen atmospheres was initially demonstrated by Iwahara and co-workers in 1981 [16]. Since then perovskites based on $BaCeO_3$, $BaZrO_3$, $SrZrO_3$, and $CaZrO_3$ [17–21] have been studied as protonic conductors. Cerate-based materials display higher protonic conductivity than zirconate-based materials [22]. Within cerates, barium cerates generally display higher protonic conductivity than strontium cerates [18]. Molecular hydrogen transport through the proton-conducting membranes can be achieved either by short-circuiting the electrodes or by applying a current across the electrodes (galvanic mode). Galvanic hydrogen permeation in $BaCe_{1-x}M_xO_{3-\delta}$ (M = Sm, Nd, Y; $x = 0.05$–0.20) oxides has been successfully demonstrated by several authors [17, 18, 23].

To achieve hydrogen permeation under open-circuit condition (non-galvanic mode) the material must display high electronic conductivity in addition to protonic conductivity. Non-galvanic hydrogen permeation through a $SrCe_{0.95}Yb_{0.05}O_{3-\delta}$ membrane has been demonstrated at 900 °C [24, 25]. In a series of studies, Qi and Lin [26, 27] demonstrated the importance of the dopant in enhancing electronic conductivity in the material, and observed non-galvanic hydrogen permeation through a $SrCe_{0.95}Tm_{0.05}O_{3-\delta}$ membrane at 900 °C. It was reported that the electronic conductivity of the doped strontium cerate increased with decreasing ionization potential of the dopants. In other words, electronic conductivity of the oxide depended on the ease with which the dopant could exhibit multiple oxidation states [27].

Cobalt, with its ability to exist in multiple oxidation states, could act as a suitable dopant to introduce electronic conductivity in protonic conductors, while also providing suitable catalytic activity for hydrogen production. However, reports to-date investigating period IV transition metal co-doping in protonic conductors have been limited to using them as sintering aids [28–30]. In one such study, McIntosh and coworkers [30] observed both protonic and electronic conductivity in $BaCe_{0.5}Zr_{0.4}Co_{0.10}O_{3-\delta}$ in the presence of hydrogen; however, this study [30] was aimed at achieving purely proton-conducting electrolytes for solid-oxide fuel-cell applications. Hence, primary investigation was limited to (Y, Yb) doped barium cerate-zirconates with 3% Co added solely as a sintering aid. In contrast, the present article details the fabrication of a mixed proton/electron-conducting material employing Co as the sole dopant to the barium cerate-zirconate perovskite. Catalytic activity of Co toward hydrogen generation reactions has been well-documented in literature. Studies have demonstrated the utility of Co-based catalysts for hydrogen generation from partial-oxidation of CH_3OH [8, 31]. Hence, Co is expected to impart sufficient catalytic activity for hydrogen generation from CH_3OH while simultaneously imparting to the barium cerate-zirconate perovskite mixed protonic–electronic conductivity for hydrogen purification.

$BaCeO_3$-based perovskite was selected as the base oxide for the investigation. Barium cerates display the highest protonic conductivity among perovskite protonic conductors investigated [18, 22]. Zirconium was added to the composition because partial substitution of Ce by Zr has been reported to improve chemical stability of barium cerates in CO_2 containing atmospheres, with an offset in protonic conductivity [22, 32]. Co was selected as the aliovalent dopant and was expected to impart mixed protonic–electronic conductivity and catalytic activity toward hydrogen generation from CH_3OH. The target composition of the material was: $BaCe_{0.25}Zr_{0.60}Co_{0.15}O_{3-\delta}$ (BCZC).

Experimental

BCZC was synthesized via the route of oxalate co-precipitation. Metal nitrates were used as precursors. Appropriate amounts of $Ba(NO_3)_2$ (Sigma–Aldrich, 99+%,

A.C.S. reagent), $Ce(NO_3)_3{\cdot}6H_2O$ (Sigma–Aldrich, 99%), $ZrO(NO_3)_2{\cdot}xH_2O$ ($x \sim 6$) (Sigma–Aldrich, tech.), and $Co(NO_3)_2{\cdot}6H_2O$ (Sigma–Aldrich, 98+%, A.C.S. reagent) were dissolved in de-ionized H_2O. Oxalic acid (Sigma–Aldrich, 98%) dissolved in de-ionized H_2O was used as the precipitant. Precursor solution was slowly added to the precipitant solution and reaction mixture was equilibrated under stirring at 50 °C and pH 2 for 2.5 h. Aqueous NH_4OH solution (Sigma–Aldrich, A.C.S. reagent, NH_3 content 28–30%) and HNO_3 (J.T. Baker # 9601) were used to set the pH of the reaction mixture. The pink precipitate was filtered out and washed with 1.5 L de-ionized H_2O followed by 0.5 L C_2H_5OH. Details of the BCZC synthesis are summarized in Table 1.

Precipitate was dried at 140 °C for 3 h to yield the as-dried powder. All heat-treatment and sintering was carried out in air on a Pt foil placed in an Al_2O_3 crucible, with heating and cooling rates of 5 °C/min. Material was held at relevant temperature for 4 h during heat-treatment and for 12 h during sintering.

X-ray diffraction (XRD), transmission and scanning transmission electron microscopy (TEM & STEM) coupled with X-ray energy dispersive spectroscopy (XEDS) were used to verify successful fabrication of the target homogeneous material. Powders heat-treated at 1,150 and 1,550 °C were characterized by XRD (Bruker Axs D5005 diffractometer, Cu-Kα radiation) over the 2θ range of 20–100° at a scan rate of 2°/min. Product heat-treated at 1,550 °C was obtained in the form of a sintered lump and was hand-ground into a powder in a mortar and pestle before using it for XRD and TEM studies. The powder was suspended in CH_3OH and ultra-sonicated for about 15 min. Five drops of suspended solution were taken onto an ultra-thin amorphous C support film for microscopic investigation. A JEOL 2010 FasTEM operated at 200 kV and Tecnai T12 TEM–STEM operated at 120 kV were used for conventional and analytical imaging, respectively. STEM imaging was carried out in nano-probe mode and the analytical XEDS mapping was performed with the same electron-optical set up. The images were drift-corrected for better accuracy and 1,000 ms residence time at each point was used for chemical mapping.

Heat-treatment temperature of 1,550 °C was determined necessary to obtain homogeneous BCZC, as detailed in the "Discussion" section of this article.

Density of sintered BCZC pellets was measured using a Mettler-Toledo density-determination kit (catalog # 33360). The procedure for preparing the pellets has been discussed later in the article. The pellets were weighed in air (A) and in C_2H_5OH (B). The temperature of C_2H_5OH was measured in order to obtain its density ($\rho_{C_2H_5OH}$); density of the material (ρ_{BCZC}) was calculated as per the following equation:

$$\rho_{BCZC} = \frac{A}{(A - B)} * \rho_{C_2H_5OH}$$

BCZC was tested for catalytic activity toward hydrogen generation via partial-oxidation of CH_3OH. As-dried powder was heat-treated at 1,550 °C and the product was broken into small pieces (<5 mm) suitable for loading into a packed-bed reactor. The reactor was comprised of a quartz reaction tube, packed with 2 g of BCZC with (20 mm depth) layers of (2 mm diameter × 2 mm length) rod-shaped quartz beads placed above and below the catalyst zone to ensure uniform distribution of reactants. Reaction temperature control was provided by an Omega CNi16D44 PID controller operating an (12.5 mm × 600 mm) Omega STH051-020 resistive-heating tape wrapped around the reaction tube; temperature was continuously monitored using an (1.5 mm outside diameter) Omega K-type thermocouple inserted into a quartz well placed in proximity to the reaction zone. Helium carrier gas, containing 5% N_2 as an internal standard, was blended with a 5% O_2/He mixture to vary O_2:CH_3OH ratios. The resulting dry gas mixture was flowed through a gas-washer filled with CH_3OH and maintained at 0 °C via immersion in an ice bath, prior to entering the reactor tube at a total flow rate of 135 mL/min. Using Raoult's law, the molar concentration of CH_3OH in the feed was estimated to be ~4%. Reaction products were stripped of H_2O and un-reacted CH_3OH using a liquid trap maintained at −78.5 °C using a dry-ice/C_2H_5OH bath. Dry product mixture was analyzed using an Agilent 3000A Micro Gas Chromatograph (GC) employing He as the carrier gas. The reaction was carried out at 400, 500, and 600 °C with the O_2:CH_3OH ratio varied between 0.1 and 0.7. A schematic of the experimental apparatus is presented in Fig. 1.

The catalyst tests at the three operating temperatures were conducted over the course of a week with a 24-h room-temperature dwelling period between the operating temperatures. This represented one run; three such runs were conducted over the course of three weeks and the data were combined to prepare the plots presented in the article.

Table 1 Synthesis details for a target of 25 g $BaCe_{0.25}Zr_{0.60}Co_{0.15}O_{3-\delta}$ (BCZC)

Reagent	Mass (g)	Notes
$Ba(NO_3)_2$	23.3	Precursors dissolved in 750 mL de-ionized water
$Ce(NO_3)_3{\cdot}6H_2O$	9.7	
$ZrO(NO_3)_2{\cdot}xH_2O$ ($x = 6$)	18.1	
$Co(NO_3)_2{\cdot}6H_2O$	3.9	
$H_2C_2O_4$	43.6	Precipitant dissolved in 750 mL de-ionized water

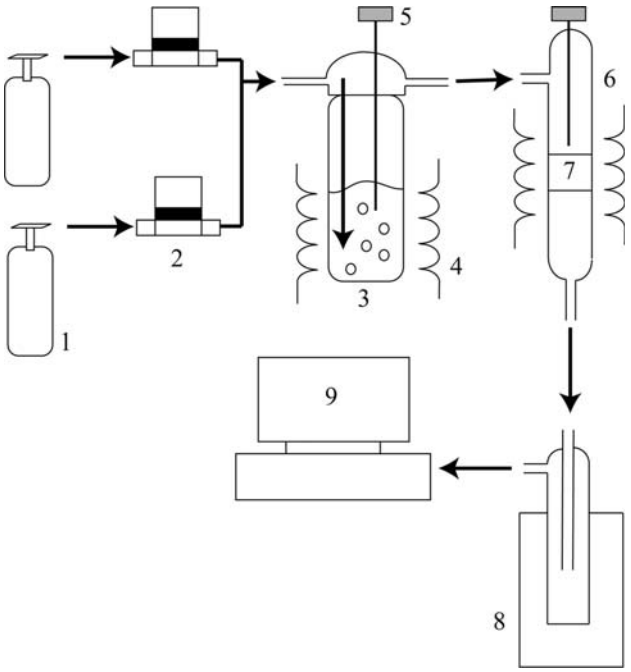

Fig. 1 Schematic of catalytic activity measurement set-up; (1) Gas cylinder (5% N_2 in He, 20% O_2 in He), (2) Mass flow controller, (3) Gas washer, (4) Heat source, (5) Thermocouple, (6) Quartz reaction tube, (7) Catalyst/quartz beads, (8) Liquid trap/ethanol-dry ice bath, and (9) GC/computer

Error bars representing 95% confidence intervals have been provided to encapsulate variations within and between runs.

Electrochemical impedance spectroscopy tests (Solartron potentiostat SI 1287, Solartron frequency response analyzer SI 1260) were conducted on BCZC pellets in different atmospheres at different temperatures with both Pt and Ag electrodes, as summarized in Table 2. As discussed below, protonic conduction can occur either by interaction of hydrogen with lattice oxygen or by interaction of H_2O with oxygen vacancies. Electronic conductivity was determined by impedance spectroscopy in dry, inert gases to eliminate ionic charge carriers in the atmosphere. Hence, dry N_2/He, wet N_2/He, and wet N_2/He/hydrogen were selected as atmospheres for the impedance spectroscopy measurements.

All tests were conducted in the frequency range 1 MHz to 0.1 Hz with A.C. amplitude of 10 mV. Results were obtained in terms of real and imaginary components of impedance (Z' and Z'', respectively), frequency (f Hz), and phase angle (θ^{o}). Cylindrical pellets (13 mm die) were made by cold-pressing hand-ground BCZC powder at a pressure of approximately 210 MPa. The pellets were then sintered at 1,550 °C. Both faces of the sintered pellets were polished with abrasive paper (Buehler Ltd., Grit 400/P 800). A schematic of the impedance measurement set-up is presented in Fig. 2.

The electrode consisted of a flat circular Pt spiral spot-welded to a Pt mesh (52 mesh, woven from 0.1 mm diameter wire). The BCZC pellet was sandwiched between two such mesh/spiral electrodes inside a quartz tube-in-tube set-up with provision to maintain desired atmosphere around the pellet. Platinum wires (0.5 mm diameter) were used as current collectors. Compression was the only means used to establish electrode–electrolyte contact. The set-up was inserted into a Carbolite MTF 12/38/250 electric tube-furnace for temperature control. For wet atmospheres, dry gas was flowed through a gas-washer filled with de-ionized H_2O maintained at 30 °C. Temperature control was provided by an Omega CNi3244 PID controller operating an (12.5 mm × 600 mm) Omega STH051-020 resistive-heating tape wrapped around the gas-washer; temperature was continuously monitored using an (6.25 mm outside diameter) Omega K-type thermocouple immersed in the liquid phase.

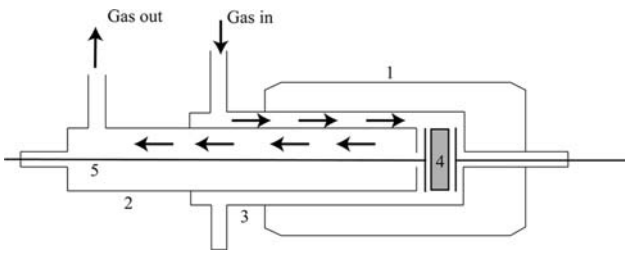

Fig. 2 Schematic of impedance measurement set-up; (1) Tube furnace, (2) Inner quartz tube, (3) Outer quartz tube, (4) Pellet, and (5) Wire (spiral/mesh electrode attached at one end)

Table 2 Details of impedance spectroscopy tests

Electrode material	Test #	Atmospheres**	Pellet dimensions (mm)
Pt	Pt-1	Dry N_2/He	$d \sim 12.26$
		Wet 10% H_2 in N_2/He	$t \sim 2.08$
Pt	Pt-2	Dry N_2/He	$d \sim 12.30$
		Wet N_2/He	$t \sim 2.05$
		Wet 10% H_2 in N_2/He	
Ag	Ag-1	Dry N_2/He	$d \sim 12.26$
		Wet N_2/He	$t \sim 2.09$
		Wet 10% H_2 in N_2/He	

$d \rightarrow$ diameter, $t \rightarrow$ thickness

** Water vapor partial pressure in all wet atmospheres was approximately 4.2 kPa

Each test was conducted using the following procedure: the furnace was brought to 400 °C, equilibrated for 30 min, and five impedance measurements were recorded. Temperature was increased to 500 °C (and then 600 °C) at 5 °C/min and five impedance measurements were recorded after 30 min equilibration. This cycle was repeated six times for dry and wet N_2/He and seven times for wet hydrogen. Three cycles were recorded daily; all overnight equilibration was performed at 200 °C.

Discussion

An XRD pattern obtained for powder heat-treated at 1,150 °C is presented in Fig. 3. Analysis of the pattern indicates that the material was comprised of two different cubic phases. Peaks denoted by the asterisk (*) match pattern reported for $BaCeO_3$ ($a = 4.37$ Å) [33] and peaks denoted by the dagger (†) match pattern reported for $BaZrO_3$ ($a = 4.18$ Å) [33]. An XRD pattern obtained for powder heat-treated at 1,550 °C is presented in Fig. 4. The pattern could be indexed with a high degree of accuracy to a single cubic phase with $a = \sim 4.28$ Å. Peaks in the observed pattern corresponded closely to those in the aforementioned patterns for $BaCeO_3$ and $BaZrO_3$ but were shifted in 2θ values such that $a(BaZrO_3) < a(1550) < a(BaCeO_3)$; this observation is consistent with results reported for barium cerate-zirconates [32], with the decrease in lattice parameter of barium cerate attributed to substitution of Ce^{4+} ion (87 pm [34]) by the smaller Zr^{4+} (72 pm [34]) ion. Observations in the present investigation are consistent with a study which reported that a heat-treatment temperature greater than 1,500 °C was required for obtaining single-phase barium cerate-zirconate from material synthesized using oxalate co-precipitation [35]. Based on the ionic radii of Co^{2+} (75 pm [34]), Co^{3+} (55 pm [34]), Zr^{4+} (72 pm [34]), Ce^{4+} (87 pm [34]), and Ba^{2+} (161 pm [34]) it can be argued, using Pauling's rules, that Co ions did not substitute for Ba ions on the A-sites and therefore either substituted for Zr/Ce ions on the B-sites or were positioned in other interstitial sites in the cubic lattice structure.

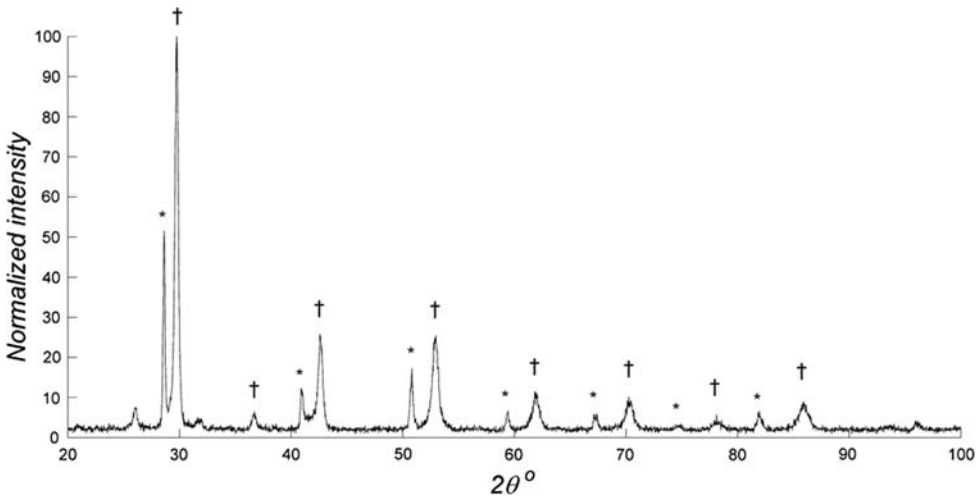

Fig. 3 XRD pattern for powder heat-treated at 1,150 °C, (* $BaCeO_3$ [JCPDS 75-0431], † $BaZrO_3$ [JCPDS 74-1299])

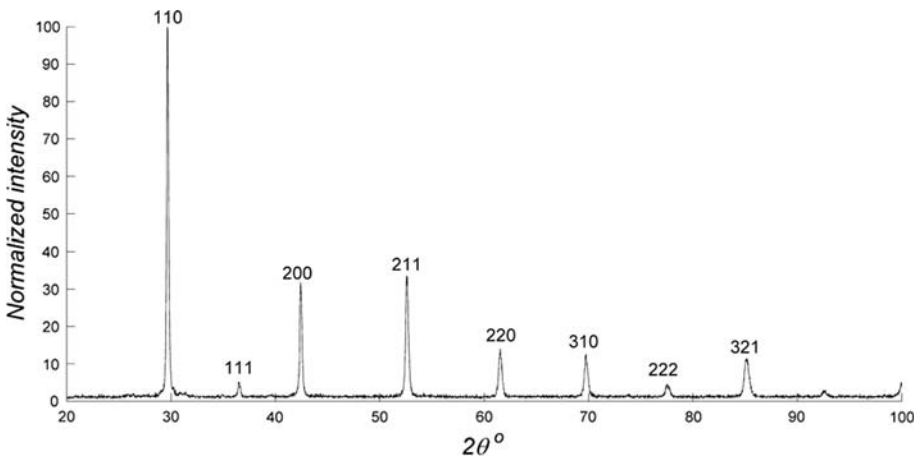

Fig. 4 XRD pattern for powder heat-treated at 1,550 °C

Values of *d*-spacing measured from the electron-diffraction pattern closely match with the XRD result (Table 3). Multiple concentric Debye rings were observed in the electron-diffraction patterns, indicating the polycrystalline nature of the sample. Electron-diffraction pattern obtained for powder heat-treated at 1,550 °C is given in Fig. 5. The dimensions of the crystalline particles after heat-treatment at 1,550 °C are micrometer (1–10 μm) in size. In order to determine the chemistry of the particles, STEM-XEDS analytical mapping was carried out on several particles. The chemistry of the particles is complicated, and the X-ray spectra of many of the elements are very close. For mapping, independent energy windows were chosen. The image of a particle and the corresponding analytical maps for Ba, Ce, Zr, and Co are given in Fig. 6. As it is evident from the figure, the elements are homogeneously distributed without any signature of localized segregation up to nanometer length scale. XEDS spectrum from a large area of the sample is given in Fig. 7. It is observed from the figure that all the elements were present in the sample without detectable contamination. This confirms that the synthesized material was contamination-free and homogeneous as found by electron-microscope measurements. As the functional properties are sensitive to phase structure and chemistry, this result strongly supports the proposal that the catalytic and functional properties of this material were not due to the presence of any unwanted impurity. The Cu signal is attributed to the TEM support grid. Density measurements of BCZC pellets yielded an average sintered density of 6.18 g/cm^3.

BCZC was tested for catalytic activity toward hydrogen generation via partial-oxidation of CH_3OH at different temperatures and O_2:CH_3OH ratios and the products were analyzed on a dry basis using a GC. Hydrogen, CO, CO_2, and CH_4 were detected in the product mixture. N_2 was used as an internal standard for calculating the outlet flows of the products. Product yield was calculated by Eq. 1.

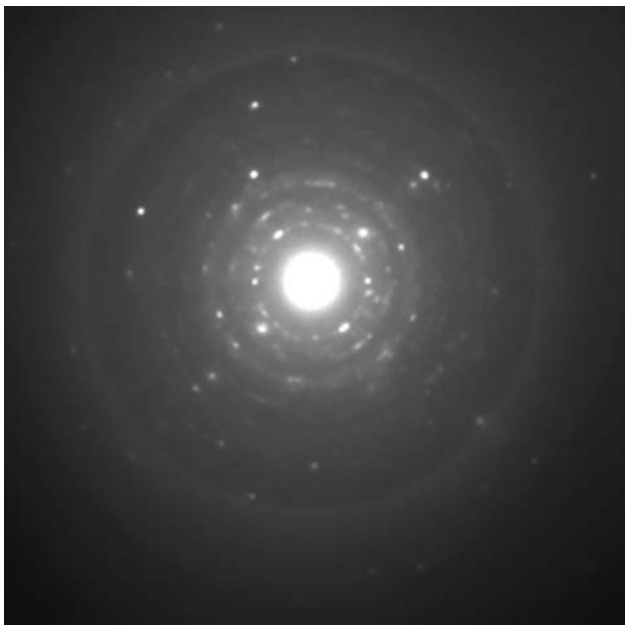

Fig. 5 Electron-diffraction pattern for powder heat-treated at 1,550 °C

$$Y_i = \frac{\varepsilon_i \cdot F_i}{F_{CH_3OH,inlet}} \quad (1)$$

where Y_i is the yield of species i (CO, CO_2, CH_4, hydrogen), ε_i is the stoichiometric coefficient for each species (=1 for CO, CO_2, CH_4; =½ for hydrogen), F_i is the outlet molar flow rate of species i, as calculated via gas chromatography, and $F_{CH_3OH,inlet}$ is the molar feed rate of CH_3OH, as calculated from the CH_3OH gas-washer temperature. CH_3OH conversion was determined by applying a C mass balance over the system (Eq. 2).

$$X = 1 - \frac{F_{CH_3OH,inlet} - F_{CO} - F_{CO_2} - F_{CH_4}}{F_{CH_3OH,inlet}} \quad (2)$$

Results of the CH_3OH partial-oxidation experiments are presented in Figs. 8, 9, 10, and 11. In a catalytic CH_3OH

Table 3 Reported and measured *d*-spacing values

Reported *d*-spacing values ($BaCeO_3$) [34]	Calculated *d*-spacing values (BCZC-XRD)	Calculated *d*-spacing values (BCZC-TEM)	Reported *d*-spacing values ($BaZrO_3$) [34]
3.10	3.04	3.03	2.96
2.53	2.48	2.85	2.41
2.19	2.14	2.15	2.09
1.96	–	1.92	1.87
1.79	1.75	1.78	1.71
1.55	1.51	–	1.48
1.46	–	–	1.39
1.39	1.35	–	1.32
1.32	–	–	1.26
1.26	1.23	–	1.21

All *d*-spacing values are in Å

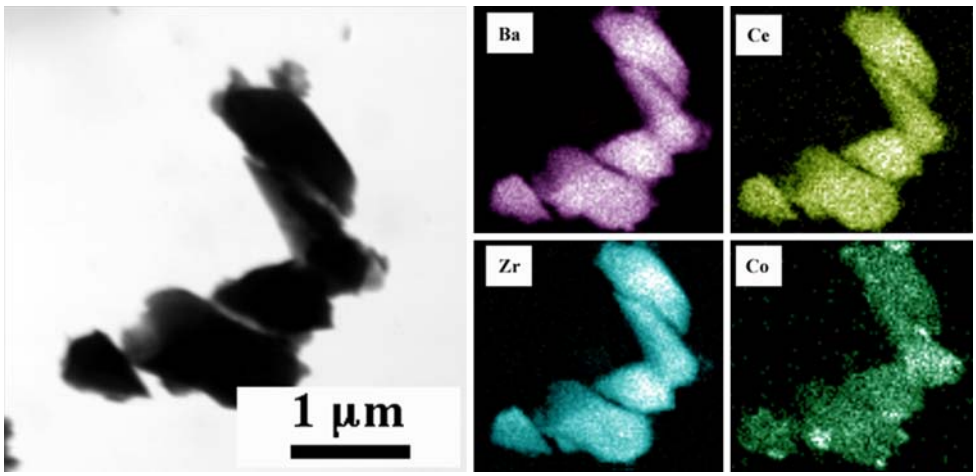

Fig. 6 STEM image and STEM-XEDS maps of Ba, Ce, Zr, and Co of the powder heat-treated at 1,550 °C. Homogeneous distribution of the elements is clearly visible

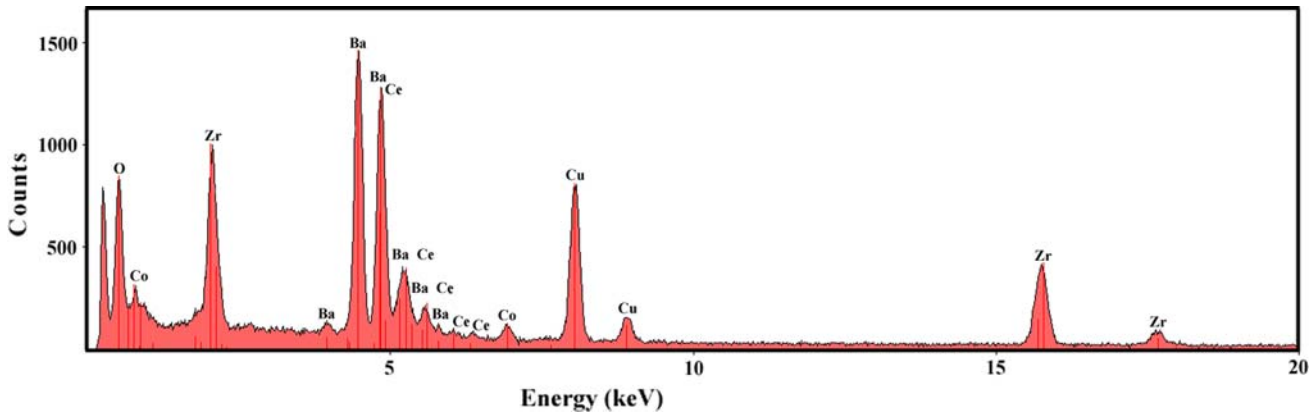

Fig. 7 TEM large area XEDS from the sintered sample showing the presence of all elements and the absence of impurities

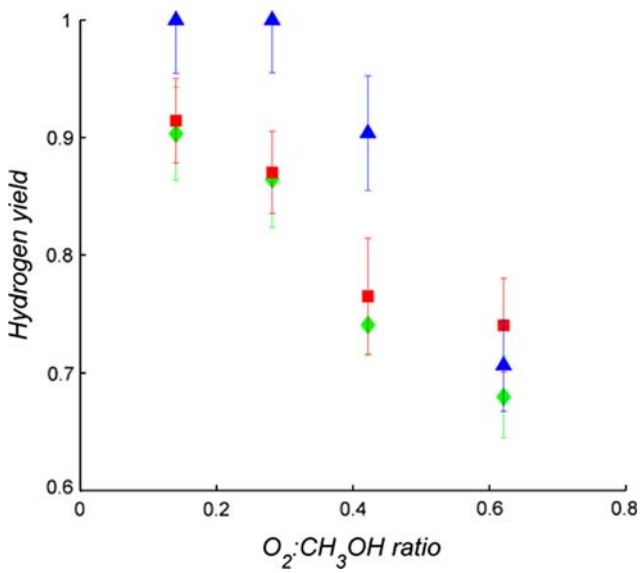

Fig. 8 H_2 yield vs. O_2:CH_3OH ratio, (*diamond*—400 °C, *square*—500 °C, and *triangle*—600 °C)

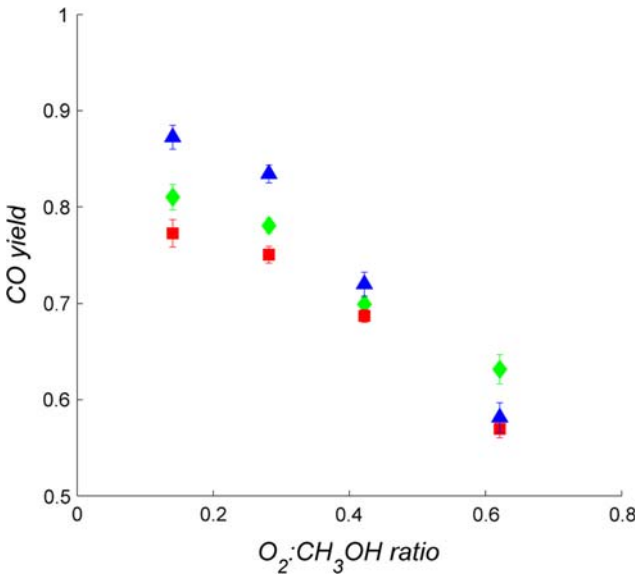

Fig. 9 CO yield vs. O_2:CH_3OH ratio, (*diamond*—400 °C, *square*—500 °C, and *triangle*—600 °C)

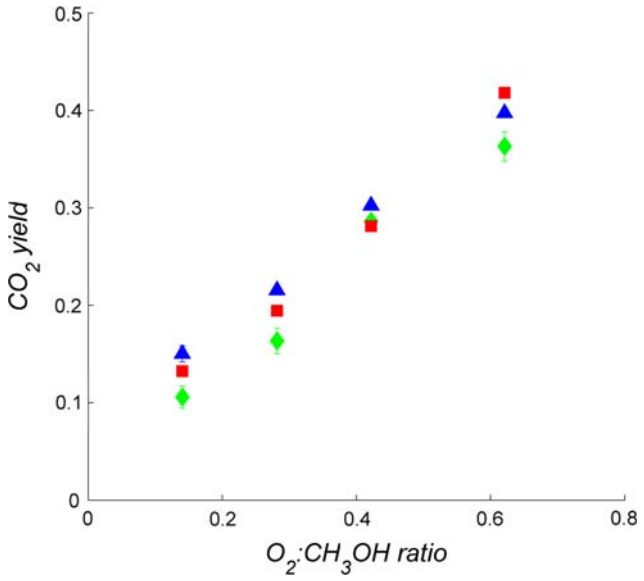

Fig. 10 CO_2 yield vs. O_2:CH_3OH ratio, (*diamond*—400 °C, *square*—500 °C, and *triangle*—600 °C)

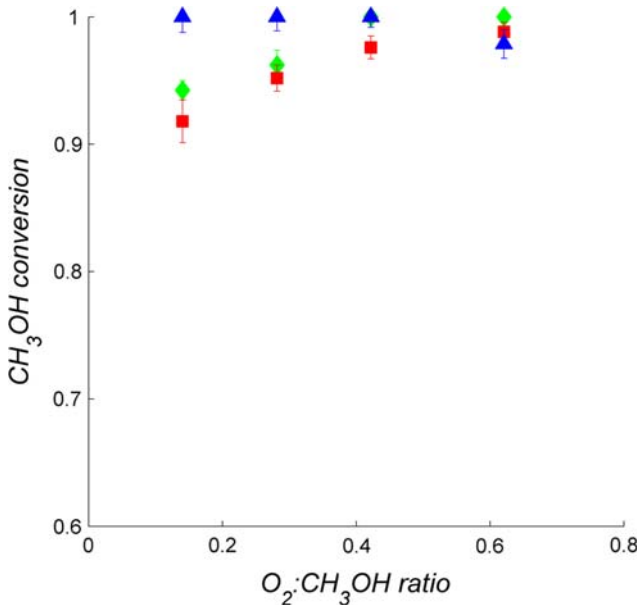

Fig. 11 CH_3OH conversion vs. O_2:CH_3OH ratio, (*diamond*—400 °C, *square*—500 °C, and *triangle*—600 °C)

partial-oxidation reaction the hydrogen and CO yields would be expected to decrease with increasing O_2:CH_3OH ratios whereas the CO_2 yields would be expected to increase with increasing O_2:CH_3OH ratios. These trends would be indicative of an increasing shift from partial-oxidation to combustion, with increasing O_2:CH_3OH ratios.

$$\text{Partial oxidation: } CH_3OH + \frac{1}{2}O_2 \leftrightarrow CO_2 + 2H_2$$

$$\text{Combustion: } CH_3OH + \frac{3}{2}O_2 \leftrightarrow CO_2 + 2H_2O$$

Figures 8, 9, and 10 clearly indicate that such trends, with respect to hydrogen, CO, and CO_2 yields, respectively, were observed at all three temperatures—400, 500, and 600 °C. Figure 8 indicates that hydrogen yields ranging from 60% to greater than 90% were observed over the range of (temperature/O_2:CH_3OH ratio) conditions studied. Figure 11 indicates that at 400 and 500 °C CH_3OH conversion increased from approximately 90% to almost 100% with increasing O_2:CH_3OH ratios; at 600 °C complete CH_3OH conversion was observed at all the O_2:CH_3OH ratios.

The results reported above—trends, hydrogen yields, and CH_3OH conversions—indicate that BCZC is a potential catalyst for hydrogen generation from CH_3OH partial-oxidation.

A comparison of the performance of BCZC with some other catalysts reported for CH_3OH partial-oxidation has been presented in Table 4. The hydrogen yield for BCZC at 400 °C and O_2:CH_3OH ratio of 0.28 was transformed to selectivity using the relationship: yield = conversion × selectivity. The CH_3OH conversion at this set of conditions was 0.96.

Impedance spectroscopy was conducted on samples under different temperature/atmosphere/electrode-material conditions and results were recorded as Nyquist (Z'' vs. Z') plots. In this work, analysis of Nyquist plots was the only method used to ascertain the nature of conduction in the material.

Representative plot obtained under dry N_2/He is presented in Fig. 12. Nyquist plots under dry N_2/He started with a high-frequency tail along the positive imaginary axis (Z''). This tail is attributed to inductance of the instrument leads. The plots ended in a low-frequency real-axis intercept (Z' at 0.1 Hz), which represents a pure resistive component. Due to the absence of any other feature on the Nyquist plot, this intercept was attributed to the bulk electrical resistance of the electrolyte. Intercept values decreased with increasing temperature, suggesting that electrical conduction in the material was non-metallic in nature. These observations and trends were common to both Pt and Ag electrodes. Given the absence of the

Table 4 Comparison of BCZC with catalysts reported for CH_3OH partial oxidation

Catalyst	Operating temperature (°C)	O_2:CH_3OH ratio	H_2 selectivity
Pd/ZnO [38]	350	0.30	96%
Au/TiO_2–Co_3O_4 [39]	250	0.30	~50%[a]
Au/ZnO/Al_2O_3 [40]	250	0.50	~60%[a]
BCZC	400	0.28	~90%

[a] After 20 min of operation

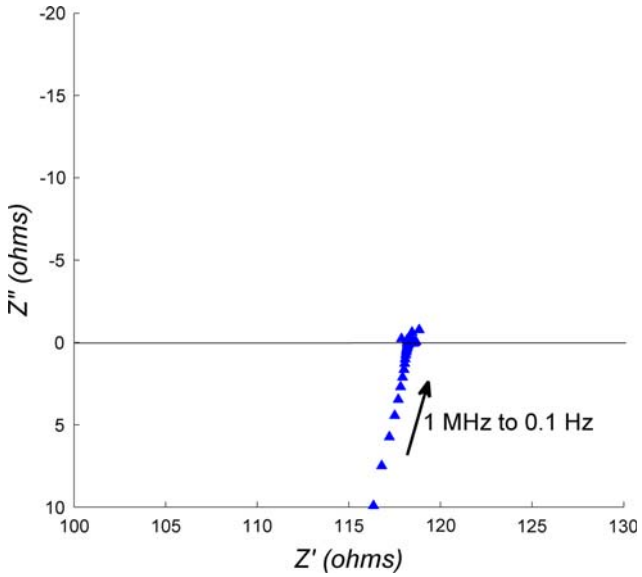

Fig. 12 Nyquist plot under dry N_2/He, 500 °C, test # Pt-2

explicit flow of air, O_2, H_2, or H_2O in the atmosphere, it can be assumed that conduction in the electrolyte under dry N_2/He would predominantly be electronic (or via electron-holes); thus the intercepts can be assigned to electronic conductivity within the material.

Under conditions where the electrolyte acts as an ionic conductor, Nyquist plots obtained with symmetrical cells typically consist of overlapping arcs. The high-frequency arc may be attributed to conduction processes occurring in the bulk or grain interior of the electrolyte. Toward the low-frequency end of the bulk-conductivity arc there may be an overlapping arc representing the motion of charged species across or along grain boundaries [36]. As the operating temperature is increased, depending on the exact sample, grain-boundary and bulk-conductivity arcs may diminish to a point where they can no longer be accurately modeled, or the characteristic frequency of the arcs may be higher than the frequency attainable by the equipment [32]. The low-frequency arc may be attributed to charge-transfer processes occurring at the electrode/electrolyte interface. Displacement of the arcs from the origin on the real axis may be attributed to unavoidable impedances associated with cell design and may be lumped into one component (Z_c) during modeling [36, 37]. Slade et al. [36] suggest that these impedances affected the spectra at higher frequencies and did not affect quantitative electrolyte conductivity data. These authors [36] have reported that Z_c initially increased with increasing temperature (attributed to cell impedances affecting the spectra more at higher temperatures) and then decreased with further increase in temperature (attributed to increased electrolyte conductivity). In the current work, Z_c values decreased from 400 to 600 °C under wet hydrogen for both electrode materials (Figs. 14, 15). Under dry N_2/He (at all three temperatures), and under wet N_2/He (at 600 °C), Z_c could not be distinguished from the electrolyte resistance and the intercepts were wholly attributed to the electrolyte.

Nyquist plots obtained under wet N_2/He are presented in Fig. 13. At 600 °C plots were similar in shape to those under dry N_2/He. However, at 400 and 500 °C the plots differed by the presence of a high-frequency arc following the inductance tail. Neither mid-frequency grain-boundary arc nor low-frequency charge-transfer arc was visible and the spectra were dominated by the high-frequency bulk-conductivity arc. In the presence of water vapor, the following reaction is expected to occur:

$$H_2O + V_O^{\bullet\bullet} + O_O^X = 2OH_O^{\bullet} \quad \text{(I)}$$

At 400 and 500 °C there appeared to be an ionic component which contributed to the electrolyte conductivity as manifested by the arc in the plots; this component, that was attributed to protons (attached to lattice oxygen ions), was generated as per Reaction I. At 600 °C, the high-frequency arc completely disappeared, possibly due to its characteristic frequency being greater than the maximum frequency used in the test (1 MHz).

Nyquist plots obtained under wet hydrogen are presented in Fig. 14. Introduction of hydrogen drastically changed the nature of the plots in comparison to dry and wet N_2/He. The plots comprised of a high-frequency bulk-conductivity arc and a low-frequency charge-transfer arc. The mid-frequency grain-boundary arc was not apparent at any of the three temperatures. In the presence of hydrogen the following reaction is expected to occur:

$$H_2 + 2O_O^X = 2OH_O^{\bullet} + 2e' \quad \text{(II)}$$

Plots (Fig. 14a–f) suggest that the introduction of hydrogen contributed significant protonic conductivity to the electrolyte via Reaction II.

Experiments were conducted with Ag electrodes to investigate whether or not the activity of the electrolyte in the presence of hydrogen was solely due to the presence of Pt as electrodes. The experimental set-up with Ag electrodes was similar to that used with Pt with the exception that the mesh was attached to the spiral using Ag adhesive conductive paste. Nyquist plots observed with Ag electrodes were similar in shape to those observed with Pt electrodes under all atmospheres. Nyquist plots obtained under wet hydrogen are presented in Fig. 15 and compared to plots from test # Pt-2. Plots obtained with Ag electrodes exhibit the same general shape as those obtained with Pt electrodes, indicating that similar processes occurred with respect to the electrolyte irrespective of the electrode.

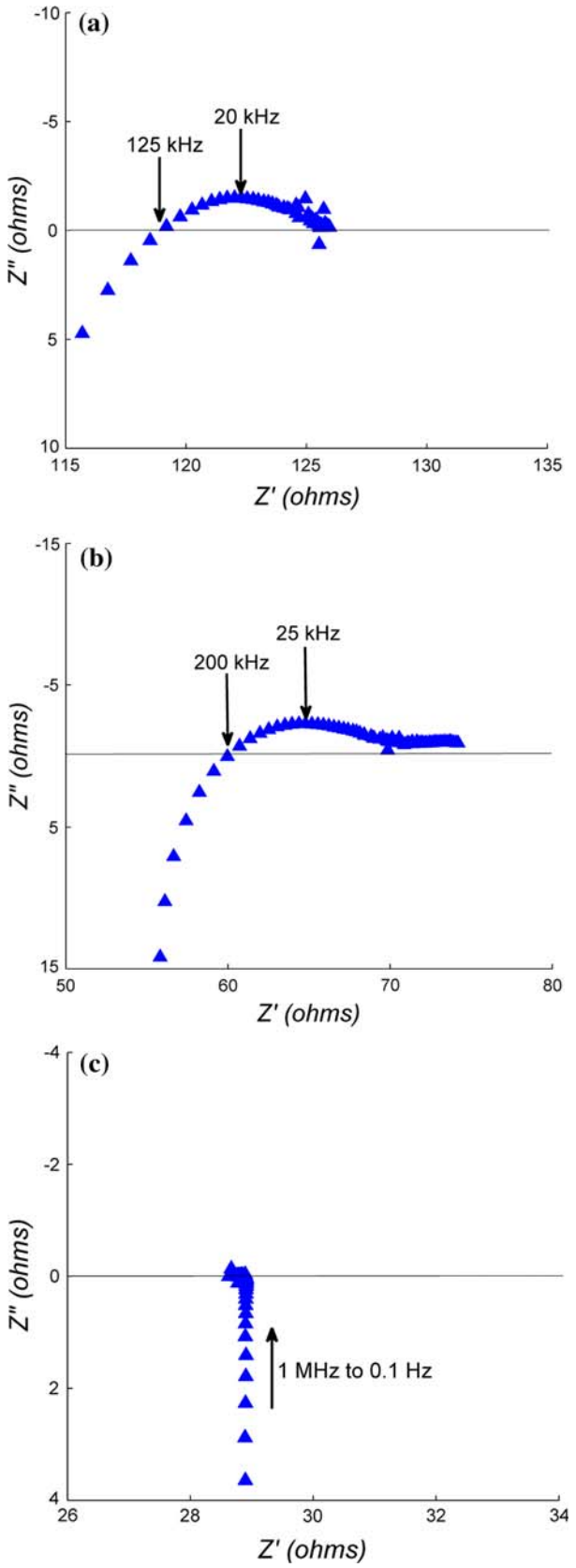

Fig. 13 Nyquist plots under wet N_2/He, **a** 400 °C, **b** 500 °C, and **c** 600 °C, test # Pt-2

Visual inspection of the plots indicates that charge-transfer resistance was much higher in the case of Ag electrodes at 400 °C.

Electronic conductivity in BCZC under dry N_2/He was estimated to be 3.8 mS/cm at 600 °C (test # Pt-1). Conductivity was estimated using Eq. 3,

$$\sigma = \frac{t}{A \cdot R} \tag{3}$$

where A is the pellet surface area, t is the pellet thickness, and R is taken as the low-frequency x-intercept (Z' at 0.1 Hz) from the Nyquist plots. Qi and Lin [27] have estimated the electronic conductivity in Tm-doped $SrCeO_3$ under pure O_2 to be 12.9 mS/cm at 800 °C (negligible oxygen-ion conductivity) and have also demonstrated non-galvanic hydrogen permeation through a membrane of the material. Since BCZC displays comparable electronic conductivity at lower temperatures and ionic conductivity in the presence of hydrogen, it is a promising candidate for hydrogen permeation by means of mixed protonic–electronic conductivity.

Conclusion

The present study demonstrates the applicability of a cobalt-doped barium cerate-zirconate perovskite electro-ceramic as a homogeneous mixed proton–electron conducting material for simultaneous hydrogen generation and purification. $BaCe_{0.25}Zr_{0.60}Co_{0.15}O_{3-\delta}$ (BCZC) was synthesized via the route of oxalate co-precipitation. XRD and TEM analyses verified the production of a single, cubic perovskite-structured phase when heat-treated at a temperature of 1,550 °C. STEM elemental maps, supported by the absence of Co-related XRD peaks, indicated that Co was distributed homogeneously within the cubic lattice. Catalytic activity of BCZC towards hydrogen generation by a CH_3OH partial-oxidation reaction was tested in the temperature range 400–600 °C and O_2:CH_3OH ratio range 0.1–0.7. Hydrogen yields greater than 60% were obtained at all reaction conditions, demonstrating the potential value of this material for hydrogen production. Tests, using electrochemical impedance spectroscopy, were conducted on BCZC pellets in the temperature range 400–600 °C, to identify possible mechanisms of electrical conduction in the material. Results indicated that BCZC exhibited substantial electronic conductivity in a dry inert atmosphere and protonic conductivity in a wet hydrogen atmosphere, making it a promising mixed protonic–electronic conductor for combined hydrogen production and purification applications. Non-galvanic hydrogen permeation through BCZC pellets is being investigated by the authors in order to fully verify the presence of mixed protonic–electronic conductivity in the material.

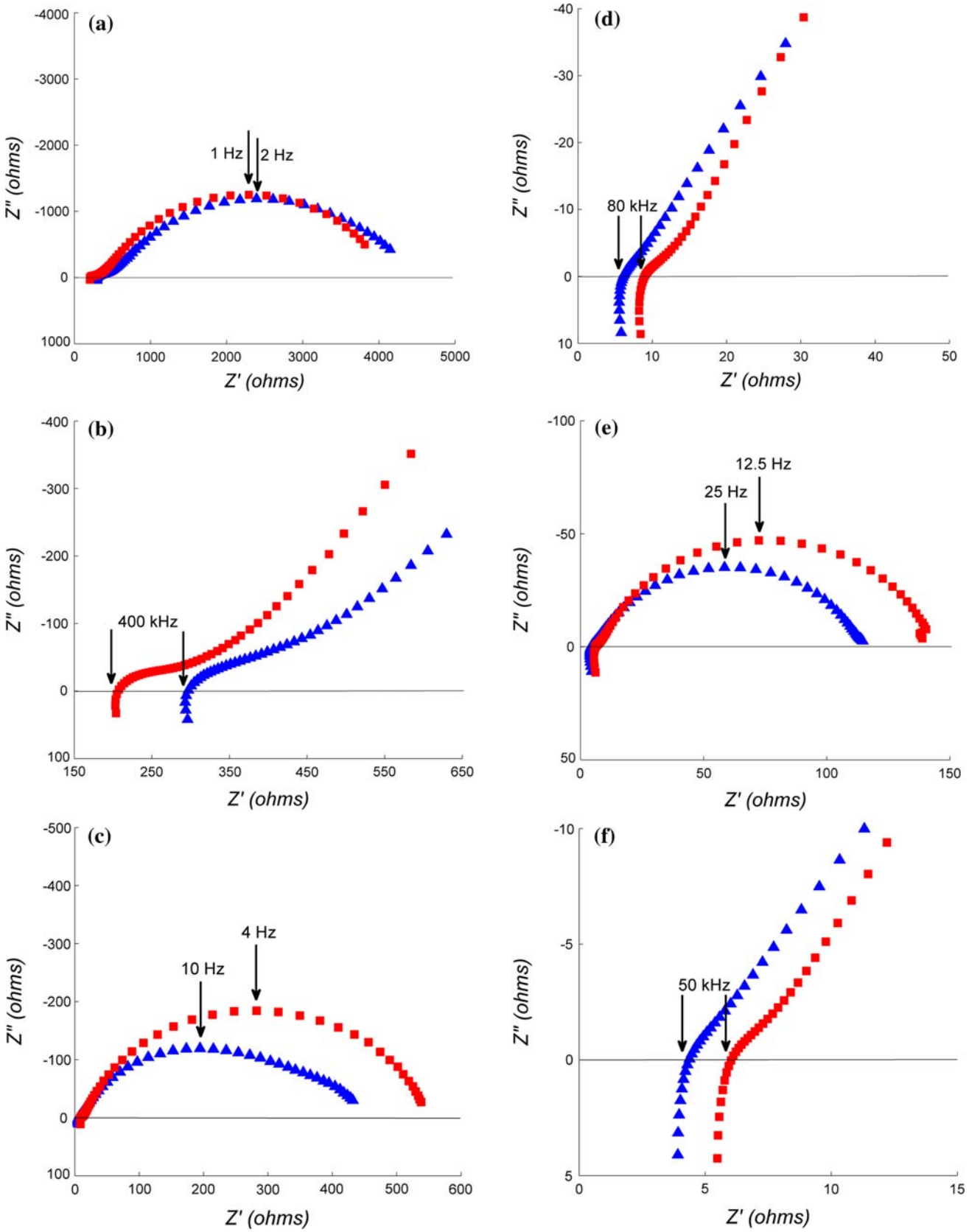

Fig. 14 Nyquist plots under wet H_2 in N_2/He, (**a**, **b**) 400 °C, (**c**, **d**) 500 °C, and (**e**, **f**) 600 °C; (**b**), (**d**), and (**f**) are zoomed-in views of high-frequency intercepts, (*square*—test # Pt-2, *triangle*—test # Pt-1)

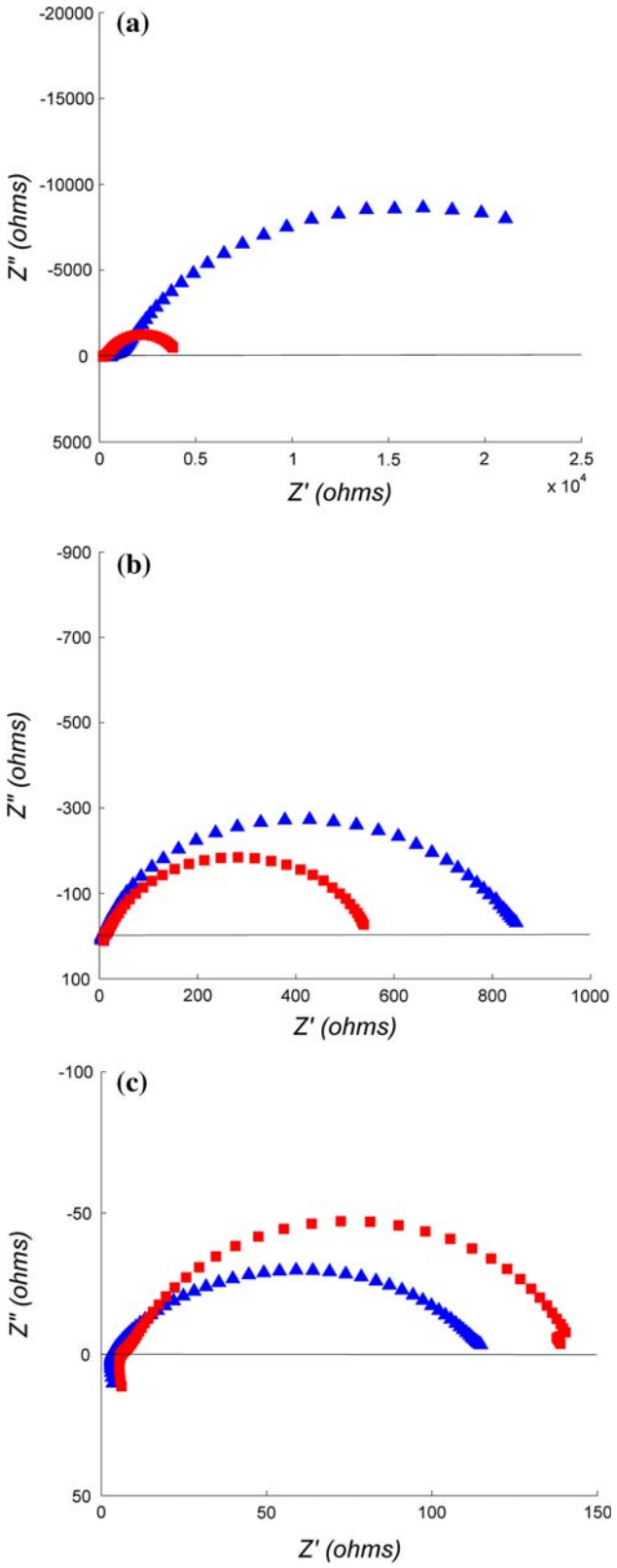

Fig. 15 Nyquist plots under wet H_2 in N_2/He, **a** 400 °C, **b** 500 °C, and **c** 600 °C, (*square*—test # Pt-2, *triangle*—test # Ag-1)

Acknowledgements The authors gratefully acknowledge Peter Menard of the Center for Clean Energy Engineering, Bill Mustain, and Jodie Lutkenhaus (of Yale University) for their valuable aid with the electrochemical analysis, and Jonathan Winterstein and Prabhakar Singh for helpful discussion. AS and BAW gratefully acknowledge the support of a 2007 DuPont Young Professor Grant and a Doctoral New Investigator Award from the American Chemical Society-Petroleum Research Fund.

References

1. Sahaym U, Norton MG (2008) J Mater Sci 43:5395. doi: 10.1007/s10853-008-2749-0
2. Larminie J, Dicks A (2003) Fuel cell systems explained, 2nd edn. Wiley, New York
3. Qi Z, He C, Kaufman A (2002) J Power Sources 111:239
4. de Briujn FA, Papageorgopoulos DC, Sitters EF, Janssen GJM (2002) J Power Sources 110:117
5. Lin Y-M, Rei M-H (2001) Catal Today 67:77
6. Ferreira-Aparicio P, Benito M, Kouachi K, Menad S (2005) J Catal 231:331
7. Paglieri SN, Way JD (2002) Sep Purif Methods 31:1
8. Wilhite BA, Weiss SE, Ying JY, Schmidt MA, Jensen KF (2006) Adv Mater 18:1701
9. Wilhite BA, Schmidt MA, Jensen KF (2004) Ind Eng Chem Res 43:7083
10. Li A, Liang W, Hughes R (2000) J Membr Sci 165:135
11. Masel R (2006) Nature 442:521
12. Hollein V, Thornton M, Quicker P, Dittmeyer R (2001) Catal Today 67:33
13. Wilhite BA (2009) In: Mitsos A, Barton P (eds) Microfabricated power generation devices: design and technology. Wiley, New York
14. Kulprathipanja A, Alptekin GO, Falconer JL, Way JD (2005) J Membr Sci 254:49
15. Sanchez Marcano JG, Tsotsis TT (2002) Catalytic membranes and membrane reactors. Wiley, New York
16. Iwahara H, Esaka T, Uchida H, Maeda N (1981) Solid State Ionics 3–4:359
17. Iwahara H, Yajima T, Hibino T, Ushida H (1993) J Electrochem Soc 140:1687
18. Iwahara H, Uchida H, Ono K, Ogaki K (1988) J Electrochem Soc 135:529
19. Snijkers FMM, Buekenhoudt A, Cooymans J, Luyten JJ (2004) Scr Mater 50:655
20. Yajima T, Suzuki H, Yogo T, Iwahara H (1991) Solid State Ionics 51:101
21. Yajima T, Kazeoka H, Yogo T, Iwahara H (1991) Solid State Ionics 47:271
22. Katahira K, Kohchi Y, Shimura T, Iwahara H (2000) Solid State Ionics 138:91
23. Balachandran UB, Guan J, Dorris SE, Bose AC, Stiegel GJ (1998) Development of mixed-conducting dense ceramic membranes for hydrogen separation. In: Proceedings of the fifth international conference on inorganic membranes, Nagoya, Japan
24. Hamakawa S, Hibino T, Iwahara H (1994) J Electrochem Soc 141:1720
25. Song S-J, Park H-S (2007) J Mater Sci 42:6177. doi:10.1007/s10853-006-1098-0
26. Qi X, Lin YS (1999) Solid State Ionics 120:85
27. Qi X, Lin YS (2000) Solid State Ionics 130:149

28. Babilo P, Haile SM (2005) J Am Ceram Soc 88:2362
29. Lin B, Hu M, Ma J, Jiang Y, Tao S, Meng G (2008) J Power Sources 183:479
30. Azimova MA, McIntosh S (2009) Solid State Ionics 180:160
31. Chinarro E, Jurado JR (2002) Key Eng Mat 206–213:1227
32. Ryu KH, Haile SM (1999) Solid State Ionics 125:355
33. Suresh A, Basu J, Carter CB, Sammes N, Wilhite BA (2008) Mater Res Soc Symp Proc (in press) (1126-S11-06), Boston, USA
34. Carter CB, Norton G (2007) Ceramic materials: science & engineering. Springer, New York
35. Wienströer S, Wiemhöfer HD (1997) Solid State Ionics 101–103:1113
36. Slade RCT, Flint SD, Singh N (1995) Solid State Ionics 82:135
37. Flint SD, Slade RCT (1995) Solid State Ionics 77:215
38. Cubeiro ML, Fierro JLG (1998) Appl Catal A 168:307
39. Chang FW, Yu HY, Roselin LS, Yang HC, Ou TC (2006) Appl Catal A 302:157
40. Chang FW, Lai SC, Roselin LS (2008) J Mol Catal A 282:129